Photoacoustics 41 (2025) 100669

Contents lists available at ScienceDirect

Photoacoustics

journal homepage: www.elsevier.com/locate/pacs

# Compact and full-range carbon dioxide sensor using photoacoustic and resonance dependent modes

Yifan Li [a,1], Lixian Liu [a,d,*,1], Liang Zhao [c], Xueshi Zhang [a], Le Zhang [a], Jialiang Sun [a], Huiting Huan [a,d,*], Yize Liang [a], Jiyong Zhang [b], Xiaopeng Shao [a], Andreas Mandelis [d], Roberto Li Voti [e]

[a] School of Optoelectronic Engineering, Hangzhou Insitute of Technology and State Key Laboratory of Electromechanical Integrated Manufacturing of High-performance Electronic Equipment, Xidian University, Xi'an 710071, China
[b] School of Communication Engineering, Hangzhou Dianzi University, Hangzhou 310018, China
[c] Northwest Institute of Nuclear Technology, Xi'an, Shaanxi 710024, China
[d] Center for Advanced Diffusion-Wave and Photoacoustic Technologies (CADIPT), Department of Mechanical and Industrial Engineering, and Institute for Advanced Non, Destructive and Non-Invasive Diagnostic Technologies (IANDIT), University of Toronto, Toronto M5S 3G8, Canada
[e] Dipartimento di Scienze di Base ed Applicate per l'Ingegneria, Sapienza Università di Roma, Rome 00161, Italy

ARTICLE INFO

*Keywords:*
Photoacoustic spectroscopy
Resonance frequency tracking
All-optical
Full-range
Time division multiplexing

ABSTRACT

A compact and robust optical excitation photoacoustic sensor with a self-integrated laser module excitation and an optimized differential resonator was developed to achieve high sensitivity and full linear range detection of carbon dioxide ($CO_2$) based on dual modes of wavelength modulated photoacoustic spectroscopy (WMPAS) and resonant frequency tracking (RFT). The integrated laser module equipped with three lasers (a quantum cascade laser (QCL), a distributed feedback laser (DFB) and a He-Ne laser) working in a time-division multiplexing mode was used as an integrated set of spectroscopic sources for detection of the designated concentration levels of $CO_2$. With the absorption photoacoustic mode, the WMPAS detection with the QCL and DFB sources was capable of $CO_2$ detection at concentrations below 20 %, yielding a noise equivalent concentration (NEC) as low as 240 ppt and a normalized noise equivalent absorption coefficient (NNEA) of $4.755 \times 10^{-10}$ W cm$^{-1}/\sqrt{\text{Hz}}$, and dynamic range as great as 11 orders of magnitude. Higher concentration detection ranges (20 %-100 %) of $CO_2$ were investigated using the RFT mode with an amplitude-stabilized He-Ne laser and a mechanical chopper. With the dual modes of WMPAS and RFT, the optical excitation sensor achieved full-range $CO_2$ detection, with an $R^2 \geq 0.9993$ and a response time of 5 seconds. The compact and full-range $CO_2$ sensor combines the advantages of WMPAS and RFT and offers a solution for high sensitivity, linearity and full-range $CO_2$ detection.

## 1. Introduction

$CO_2$ is a commonly encountered colorless and odorless gas, the high sensitivity and full-range detection capability of which through appropriate instrumentation and measurement methodologies has become a growing requirement due to its wide range of applications in industrial production, biomedicine, monitoring of environmental pollutants, and atmospheric chemistry [1–4], to name a few. In microbiological environments, such as those for fungi cultivation, the precise control of $CO_2$ concentrations to parts per million (ppm) or even parts per billion (ppb) levels is imperative[5–7]. The gaseous environment is a very important factor for ensuring the proper survival of the fungus. Therefore, the quantitative analysis of low-concentration $CO_2$ is of great importance to the biological field [8–12]. Additionally, in industrial settings, $CO_2$ levels may reach alarming concentrations ranging from 1 % to 15 % due to coal combustion and gas leakage [13,14]. Such a high concentration of $CO_2$, compared to atmospheric concentrations of about 0.036 %, can lead to human breathing difficulties or even unconsciousness in people working in such environments [15]. Furthermore, medium to high concentrations of $CO_2$ emitted from factories are one of the main sources

* Corresponding authors at: School of Optoelectronic Engineering, Hangzhou Insitute of Technology and State Key Laboratory of Electromechanical Integrated Manufacturing of High-performance Electronic Equipment, Xidian University, Xi'an 710071, China.
*E-mail addresses:* lixianliu@xidian.edu.cn (L. Liu), hthuan@xidian.edu.cn (H. Huan).
[1] Y. Li and L. Liu made an equal contribution to this work.

https://doi.org/10.1016/j.pacs.2024.100669
Received 28 September 2024; Received in revised form 8 November 2024; Accepted 13 November 2024
Available online 28 November 2024

of greenhouse gases, and the monitoring of this concentration of $CO_2$ plays an important role in industrial safety and monitoring of environmental pollutants [16–20]. What's more, in factories requiring heavy metal smelting, high concentrations of $CO_2$ as a reducing agent are critical to the success of metal smelting, which makes it necessary to provide continuously high concentrations of $CO_2$ to ensure that the smelting process is carried out successfully [21–23]. This situation requires equipment to continuously and accurately monitor the $CO_2$ concentration. Therefore, there is an urgent need for the development of instrumentation and measurement methodologies targeting high sensitivity to, and full-range sensing for, $CO_2$ detection.

The purpose of gas sensors is to analyze and detect target gases in different application scenarios, and common sensor detection methods include gas chromatography, electrochemistry, metal oxidation, catalytic combustion, infrared spectroscopy, and so on. Gas chromatography can separately determine the components of target gases. It is known for its small size, high sensitivity, and high resolution. However, sensitive chromatography instruments are expensive, and the analysis time is relatively long (on the order of 3 minutes) [24]. It is also well-known that the long-term stability of these instruments needs further improvement. Electrochemical sensors face challenges such as poor selectivity in detecting various trace impurity gases and susceptibility to interference in environments like hydrogen fuel cells [25]. Metal oxide sensors exhibit unsatisfactory stability in battery applications, requiring repeated calibration and incurring high maintenance costs [26]. Catalytic combustion sensors, used to detect key impurity gases, often suffer from interference among target gases and have a short operational lifespan [27]. WMPAS technology has the advantages of low cost, high sensitivity, high selectivity, relatively small size, and real-time detection, which makes it a popular method for gas detection [28–31]. However, WMPAS tends to saturate at high concentrations and even tends to drop the signal strength, making it impossible to accomplish reliable full-range linear detection of gases [32].

There is a lack of common sensors capable of full-range gas detection. The compact $CO_2$ sensor developed in this work combines the advantages of WMPAS and RFT to provide an alternative solution for high-precision and full-range $CO_2$ detection. Most of the sensors using this mode are acousto-optic (AO) sensors, with the advantage of our comprehensive all-optical $CO_2$ sensor being that it is more widely applicable to many environments than AO sensors because light propagation does not require a propagation medium. Moreover, the optical source does not need to be in contact with the photoacoustic cell like AO sensors require.

Aiming at the fact that WMPAS is unable to complete full-range $CO_2$ gas detection, an all-optical laser source was used in our studies. By combining WMPAS and RTF techniques with this all-optical excitation method, we can detect gases in the sub-ppb range and achieve a detection limit as low as 240 ppt. This approach offers an alternative solution to RFT for high sensitivity, linearity and full-range $CO_2$ detection.

## 2. Experimental setup

### 2.1. Selection of absorption cross-section and laser source

According to the HITRAN database [33], $CO_2$ molecules exhibit strong absorption bands in the near-infrared (NIR) and mid-infrared (MIR) regions [34]. The absorption cross-section simulation results of $CO_2$ and water vapor background given in the HITRAN database at a temperature of 296 K and 1 atm pressure are presented in Fig. 1. The red lines represent the absorption intensities of $CO_2$ and the blue lines show the water vapor absorption spectra. Water vapor has fewer absorption lines in this spectral band, and would not cause spectral interference for $CO_2$ detection. The NIR wavenumber 4989.971 $cm^{-1}$ (line strength is 3.97 $\times 10^{-21}$ $cm^2$/mol) and MIR 2364.106 $cm^{-1}$ (line strength is 1.11 $\times 10^{-17}$ $cm^2$/mol) were chosen as the target wavelength for a DFB (NTT Electronics, NLK1S5EAAA) at 2004 nm and a QCL (Healthy photo, QC-Qube) at 4230 nm respectively based on WMPAS technology [35].

According to the photoacoustic theory of solids (Rosencwaig-Gersho theorem, RG theorem) [36], when light is modulated and irradiates a solid sample in the photoacoustic cell, the laser energy is absorbed by the cell wall, resulting in the generation of modulated thermal energy. The selected He-Ne laser has a wavelength of 632.8 nm, which falls within the visible light range and is not absorbed by most gases, including $CO_2$, making it universal. The spectral range of visible light sources typically covers wavelengths from about 400 nm to 700 nm, a wavelength range that is not absorbed by $CO_2$. Since the gas inside the photoacoustic cell does not absorb the laser light, the light interacts with the cell wall instead. Part of this energy is diffused inside the wall, while the remainder is transferred to the gas in contact with the walls. This interaction creates a boundary layer between the gas and the wall surface that responds thermally to temperature changes. As the incident laser light is periodically modulated, this boundary layer is also heated periodically, generating an acoustic piston effect that affects the residual gas in the photoacoustic cell [37]. This results in the production of pressure waves within the cell. These acoustic signals are then detected by a microphone. The frequency and amplitude of these acoustic waves are influenced by the properties of the gas, with changes in the resonance frequency significantly affecting the acoustic response. When the modulation frequency of the laser is the same as the resonance frequency of the photoacoustic cell, the signal in the photoacoustic cell reaches its maximum. By analyzing the magnitude of the resonance frequency, the concentration of the gas can be determined.

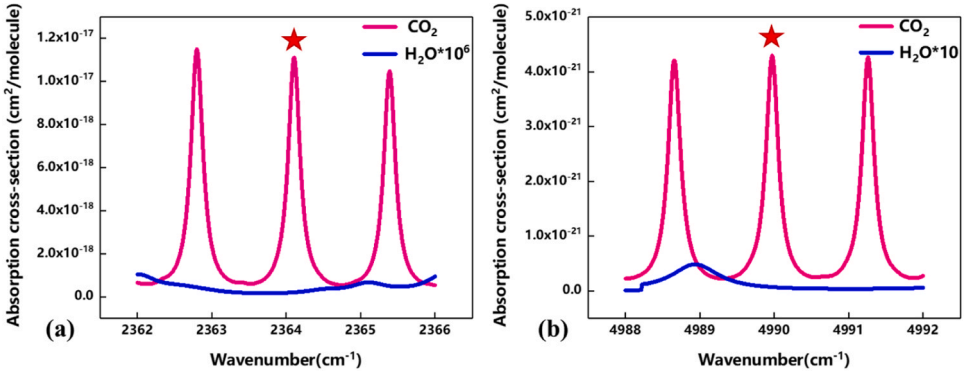


**Fig. 1.** Simulated spectral distribution characteristics of $CO_2$ and $H_2O$ based on HITRAN Database. Temperature and pressure: 296 K and 1 atm respectively. The asterisk represents the selected wavenumber.

### 2.2. Experimental setup

The schematic of the $CO_2$ sensor based on the dual modes (WMPAS and RFT) is depicted in Fig. 2.

The sensor integrates a light source unit, a self-designed control and collected unit, a photoacoustic cell unit and a gas unit. The light source unit includes QCL, DFB, and He-Ne lasers. The control and collected unit manage the laser driver, signal acquisition, modulation and demodulation, controlling the QCL, DFB, and He-Ne lasers through the control output signal $f_1$, $f_2$ and $f_3$, respectively. The QCL and DFB use the WMPAS technique, while the He-Ne laser utilizes RFT. The lasers sequentially excite the differential photoacoustic cell with two resonant cavities. Microphones (YINGLEAR, BO9745RT) with sensitivity of the microphone is −30 dB to −46 dB in the photoacoustic cell detect photoacoustic signals, enhancing the signal-to-noise ratio and ensuring sensitive gas concentration measurements. The control and collected unit perform real-time signal processing and reporting. Additionally, the gas unit includes a humidifier and a pressure controller to adjust the temperature and humidity of the gas.

For the light source unit, the core instruments include the QCL, DFB, and He-Ne lasers. The optical power of the QCL, DFB and He-Ne lasers were measured and monitored by a thermal power meter (THORLABS, PM100D) at the target absorption lines. They were found to be 54 mW, 5 mW and 22.5 mW, respectively. The three lasers were managed by the control and collection unit while the QCL and DFB were WMPAS-based and He-Ne laser is RFT-based. The wavelength-modulated beam from the QCL was emitted from left to right into the upper channel of the differential resonant cavity unit. Similarly, the beam from the DFB was launched into the lower channel from right to left through the fiber collimator. The chopper (Stanford Research Systems, SR540) was synchronized with the $f_3$ signal for modulation of the He-Ne laser in RFT mode. A He-Ne laser was fired right-to-left onto the inner wall of the upper channel of the photoacoustic cell. The three lasers were excited in a sequential order as per operational requirements.

The control and collection unit was equipped with self-designed electronics based on FPGA chips (Altera, EP4CE15F256). It was integrated in a box with dimensions of 40 × 28 × 14 $cm^3$ and a weight of 3.2 kg. It was responsible for the control of the light source unit, lock-in demodulation of PA signals and real-time-concentration calculation and reporting. The unit included a laser driver module, a signal acquisition module and a signal modulation and a demodulation module. The laser driver module was used to conduct the power supply for the laser and control the temperature and current of the laser. The signal acquisition module supplied power to the microphone above the photoacoustic cell and passed on the electrical signals collected by the microphone, outputing them to the computer to acquire the image profile. Signal modulation and demodulation modules were integrated modules that combine the functions of a signal generator, an adder and a lock-in amplifier. The sinusoidal wave and ramp signals generated in the FPGA were used for the signal modulation of the QCL, DFB and He-Ne lasers. For the setup, $f_1$ outputted a sine wave at 588 Hz and a sawtooth wave with a 20-second period. $f_2$ outputted a sine wave at 570 Hz and a sawtooth wave with a 30-second period. $f_3$ was connected to the He-Ne laser controller and a custom frequency sweeping software. The frequency of the chopper could be adjusted by varying the bias of the sine signal, which could range from 2.2 mV to 2.916 mV, resulting in a frequency sweep range from 900 Hz to 1220 Hz. Electrical signals generated by the microphone driver circuit were acquired by the signal demodulation module and were analyzed and calculated in real time with an integration time of 1 s.

The proportioned gas flowed into the photoacoustic cell unit, which in this experiment was a self-developed design. The differential photoacoustic cell consisted of two resonant cavities, each 140 mm in length and 7 mm in diameter, with buffer cavities of 30 mm length and 34 mm diameter positioned at either end. The inner wall of the resonance chamber is made of aluminum alloy and polished. The polishing of the wall not only reduces noise but also minimizes photoacoustic signal loss, preventing signal dissipation and enhancing the photoacoustic signal strength [38,39]. The inner and outer walls of the photoacoustic cell are black in color, which effectively reduces the energy loss due to reflection in the RFT mode. Additionally, Calcium Fluoride ($CaF_2$) windows were located at the ends of the buffer cavities for incident light beams. Two microphones were strategically placed at the center of the resonant cavities for detecting PA signals. In contrast to traditional H-shaped cylindrical photoacoustic cell, this differential photoacoustic cell featured two parallel resonant cavities, enhancing signal clarity and stability. This design effectively minimized external ambient noise interference and boosted the intensity of photoacoustic signals [40]. As a result, it significantly improved the signal-to-noise ratio (SNR), ensuring more reliable and accurate signal detection.

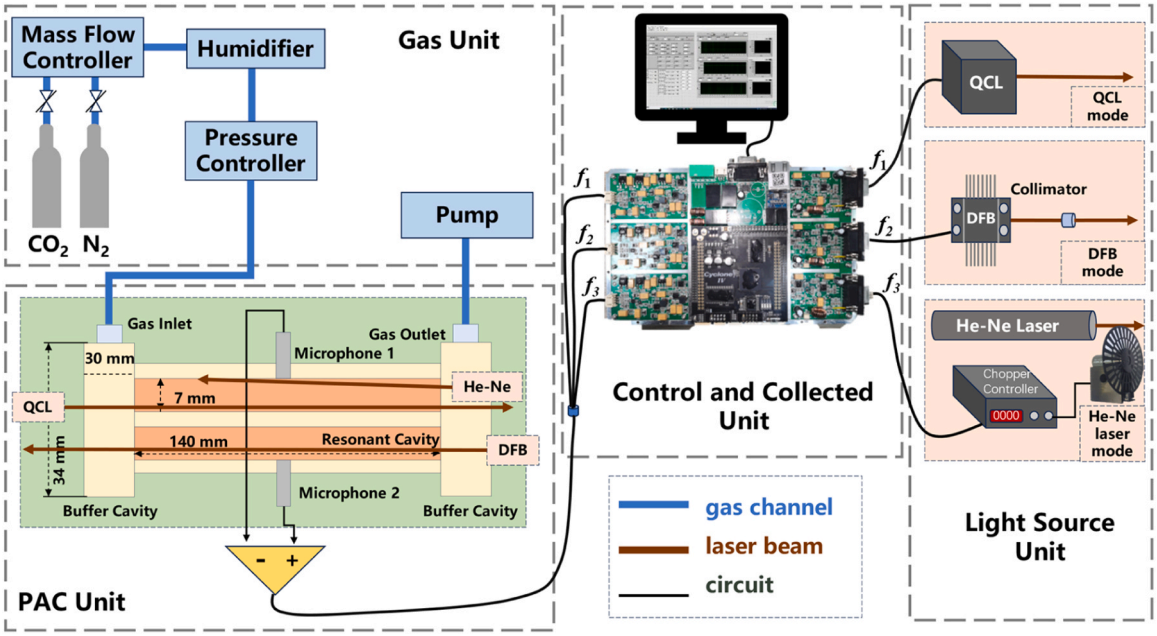


**Fig. 2.** Schematic diagram of the full-range $CO_2$ concentration sensor based on the dual modes (WMPAS and RFT).

Due to the relaxation effect of water vapor on $CO_2$ photoacoustic signal, a humidifier was introduced to add humidity or remove moisture. The flow rate was regulated using a mass flow controller and needle valves, while a pump was connected to both the resonator outlet and the end of the airflow tube. Additionally, a pressure controller (Allcat Scientific, LK 2) was positioned upstream of the resonator to maintain and control the pressure within the resonator

## 3. Optimization design of the dual mode $CO_2$ sensor

### 3.1. Simulation optimization of $CO_2$ detection range for the dual mode sensor

To achieve high sensitivity and linearity in $CO_2$ detection using the dual mode full-range sensor, careful consideration must be given to resonant frequency drift and concentration saturation effect. The simulation optimization experiments were carried out using the finite element method software COMSOL Multiphysics ®[41] v6.0 to select suitable laser light sources for various concentration intervals of $CO_2$ with a differential multichannel resonant cavity (same dimensions as the experiments). The QCL mode, DFB mode and RFT mode are simulated at 4230 nm, 2004 nm and 632.8 nm, The simulation results are shown in Fig. 3.

In WMPAS mode, based on the Lambert-Beer law, a Gaussian thermal source $I_T$ was used to imitate the laser source incident beam through the differential resonator, as shown in Eq. 1[42]

$$I_T = I_0 e^{-\alpha_{CO_2} cz} e^{-r^2/a^2} \tag{1}$$

Where $I_0$ represents the power of the laser, $I_T$ represents the transmitted power.$\alpha_{CO_2}$ denotes the absorption coefficient (0.1065 $cm^{-1}$ at the target wavelength 2004 nm for DFB and 275.6 $cm^{-1}$ at the target wavelength 4230 nm for QCL) of pure $CO_2$ and $C$ stands for the concentration of $CO_2$. The laser beam propagated along the z-axis, where $a$ is the waist radius of the Gaussian beam, $r$ represents the distance from the center axis along the beam cross-section. The parameters of the photoacoustic cell have been given in Section 2.2.

Given the high absorption coefficient of $CO_2$ at 4230 nm, the gas strongly absorbs incident laser radiation in this wavelength band, leading to saturation of the photoacoustic signal at a concentration of 60 ppm. To ensure linearity, the QCL laser was employed for detection specifically within the 0–50 ppm range (Fig. 3a).

The photoacoustic signal from 0 % to 100 % $CO_2$ exhibited a trend of initially increasing and then decreasing for the DFB mode (Fig. 3b). There was a linear relationship between concentration and photoacoustic signal within the 0–20 % region. Between the range from 20 % to 80 %, the signal increased nonlinearly. Beyond 80 %, the signal decreased.

The resonant frequency is an important performance parameter of a PA cell which is impacted by factors such as gas concentration and gas species in photoacoustic chambers, as shown in Eq. 2[43].

$$f = \nu \frac{1}{2L_{eff}} = \sqrt{\frac{\gamma RT}{M}} \frac{1}{2L_{eff}} = CV\sqrt{\frac{\gamma RT}{\mathrm{nm}}} \frac{1}{2L_{eff}} \tag{2}$$

The velocity of sound $\nu$ and the effective optical length $L_{eff}$ are related as follows[43]. The effective optical length $L_{eff}$ refers to the distance that light effectively travels through the $CO_2$ (medium) considering factors such as absorption and scattering, which represents the length of light interacting with the medium. The velocity ($v$) depends on the ratio of specific heat capacities at constant pressure and constant volume ($\gamma$), the ideal gas constant ($R$), temperature ($T$), and the molar mass of the gas ($M$). $M$ is determined by the concentration of the gas ($C$), the volume of the gas ($V$), the number of moles of the gas ($n$) and the mass of the gas ($m$). Since the temperature, pressure and gas species in the photoacoustic cell are deterministic values, the resonance frequency of the photoacoustic cell shows a positive correlation with the gas concentration. By utilizing this relationship, a curve illustrating the connection between concentration and resonant frequency allows us to determine one variable when the other is known. From Fig. 3(c), the He-Ne mode shows a linear relationship in the detection of 0–100 % concentration, but since the accuracy of RFT in low concentration detection is not as good as that of PAS, PAS is prioritized in low concentration. RFT makes up for the inability of WMPAS to achieve linear detection of high concentrations. By combining WMPAS and RFT, it becomes feasible to achieve highly accurate and full-range linear $CO_2$ detection.

Based on simulation results, concentrations were categorized into intervals where there is a linear relationship between concentration and signal. The QCL mode was utilized for detecting low concentrations (0–50 ppm), while the DFB mode handled medium concentrations (50 ppm-20 %). High concentrations (20 %-100 %) were detected using the RFT mode due to its capability of maintaining linearity in this range.

### 3.2. Optimization design of the $CO_2$ sensor

The optimization process meticulously fine-tunes key parameters such as modulation depth, flow rate and humidity levels. It aims to enhance the overall performance for achieving comprehensive $CO_2$ detection across the entire concentration range, ensuring accuracy and precision. The experiments were carried out at a temperature of 296 K and 1 atm pressure. A $CO_2$: $N_2$ gas mixture was used for the optimization experiments.

#### 3.2.1. Optimization of integrated laser

To obtain the optimal static operating current, a concentration of 20 ppm and 2 % $CO_2$ gas was used as the gas sample and the differential photoacoustic cell was excited with the QCL and the DFB in succession. The temperature of QCL and DFB was set at 25℃ and 23℃, while the center currents were set to 102 mA and 109 mA, respectively. Fig. 4 shows the relationship between the amplitude signal (a.u.) and the modulation amplitude for a QCL laser measuring 20 ppm $CO_2$ and a DFB laser measuring 2 % $CO_2$. The optimal modulation amplitudes for the

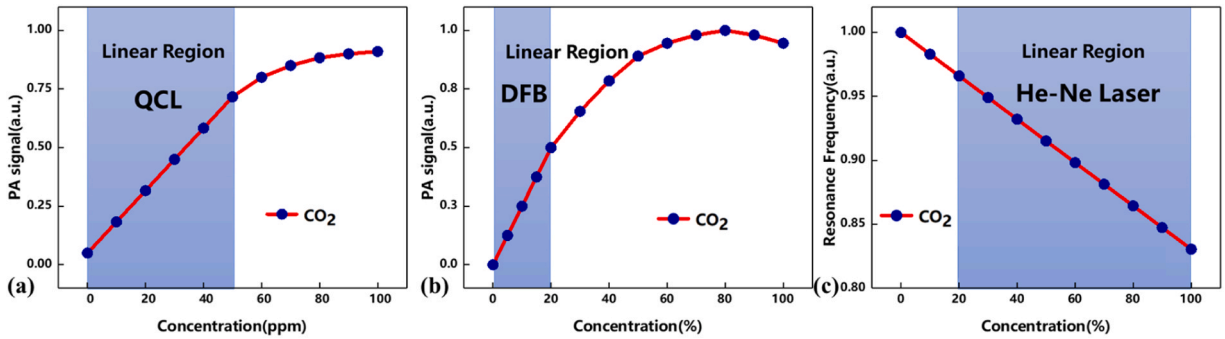


**Fig. 3.** Simulated PA signal vs. target gas concentration. (a): QCL mode (b): DFB mode (c): He-Ne Laser mode (also referred to as RFT mode).

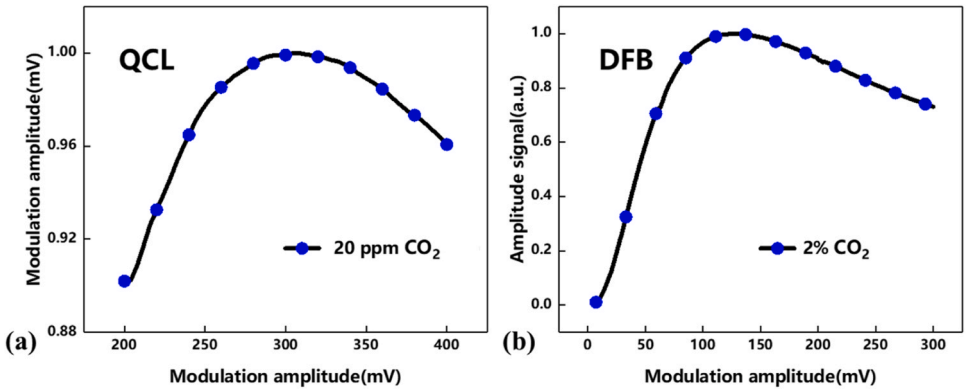


**Fig. 4.** Modulation depth curves (a):20 ppm $CO_2$ in QCL Mode (b): 2 % $CO_2$ in DFB Modulation Mode.

QCL and DFB are 308 mV and 127 mV, respectively.

The results of 2f-WMPAS spectral scanning are shown in Fig. 5. With the optimal injection current found to be 109 mA for QCL and 127 mA for DFB, the signals reached 90.2 mV and 9.8 mV at the center current, respectively. Following the optimization of the modulation depth and second harmonic, the center wavelength of lasers has been aligned with the optimal absorption lines of the target gas—4230 nm for the QCL laser and 2004 nm for the DFB laser. The center wavelength of the He-Ne laser remains fixed at 632.8 nm, as its characteristics do not require adjustment.

### 3.2.2. Optimization of gas flow rate

Flow rate is an important parameter in the experiment, as it impacts both the stability and strength of the photoacoustic signal as well as the level of background noise. Therefore, optimizing the flow rate is essential for accurate and reliable measurements.

The noise levels and PA signals of the three modes of resonator were recorded by measuring signals with 30 ppm $CO_2$, 5 % $CO_2$ and 90 % $CO_2$ as reference gases. Noise was measured at a temperature of 296 K and 1 atm pressure. The laser is turned off during the measurement. The number of accumulation points is set to 10,000 and the accumulation time is 1 s. When measuring photoacoustic signals, the optical power of the QCL, DFB and He-Ne laser were 54 mW, 5 mW and 22.5 mW, respectively. With the optimal injection current found to be 109 mA for QCL and 127 mA for DFB. He-Ne lasers have a fixed output wavelength and do not require current regulation. Experiments were performed in the flow rate range from 110 sccm to 1100 sccm. Fig. 6 shows the noise level and the PA signal. The signal for 30 ppm $CO_2$ increased with flow rate and reached a maximum at 440 sccm. The noise level stayed at 1 μV and increased dramatically to 3.2 times the original level when the flow rate was increased to 880 sccm. The 5 % $CO_2$ signal increased and then decreased as the flow rate increased, reaching a maximum at 440 sccm, followed by a slight decrease at 770 sccm. The noise level stayed at 770 sccm and then increased sharply. 90 % $CO_2$ signal reached a maximum at 550 sccm and then decreased smoothly. The noise level started to increase at 660 sccm. Therefore, 440 sccm was chosen as the optimum value for simultaneous gas measurements.

### 3.2.3. Analysis of water relaxation processes

Water vapor can be an effective catalyzer for slowly relaxing gas molecules, and thus the photoacoustic signals are greatly enhanced [42]. The samples used were gas mixtures of 50 ppm $CO_2$, 20 % $CO_2$ and 90 % $CO_2$ diluted with $N_2$, excited by QCL, DFB and He-Ne lasers in succession.

The humidification results of the 50 ppm $CO_2$ are shown in Fig. 7(a), where the photoacoustic amplitude of $CO_2$ increases significantly by about 98.95 mV/%-$H_2O$ at humidity levels above 0.325 %. When humidity increased to 2.318 %, the photoacoustic signal rose to 7.673 times its original value, reaching 197.2 mV. Fig. 7(b) shows the results for 20 % $CO_2$ measurements eusing the DFB laser, where the approximate linear increase in PA amplitude of $CO_2$ is 6.573 mV/%-$H_2O$ at humidity levels above 0.463 %. When the humidity reached 2.342 %, the photoacoustic signal increased by 12.35 mV from the initial.

Absorption lines of $H_2O$ exist in the band at target line 2364.106 $cm^{-1}$ and 4989.971 $cm^{-1}$, with line strengths of $2.506 \times 10^{-28}$ cm/mol and $3.320 \times 10^{-28}$ cm/mol, respectively. The $H_2O$ absorption line overlaps that of the target gas $CO_2$. Taking the 2364.106 $cm^{-1}$ line as an example, in the high humidity state energy is generated by the exchange of V-V collisions between $CO_2$ and $H_2O$ molecules. Thus, the vibrational energy of the excited state $\nu_3$ of $CO_2$ in the band is transferred to the $\nu_1$ rotational vibrational energy level of $N_2$[42]. (Under 4989.971 $cm^{-1}$ laser irradiation, as humidity increases, vibrational energy from the excited state $2\nu_1 + \nu_3$ of $CO_2$ transfers to the rotational-vibrational energy level $\nu_1$ of $N_2$[44].) Thus the increase of

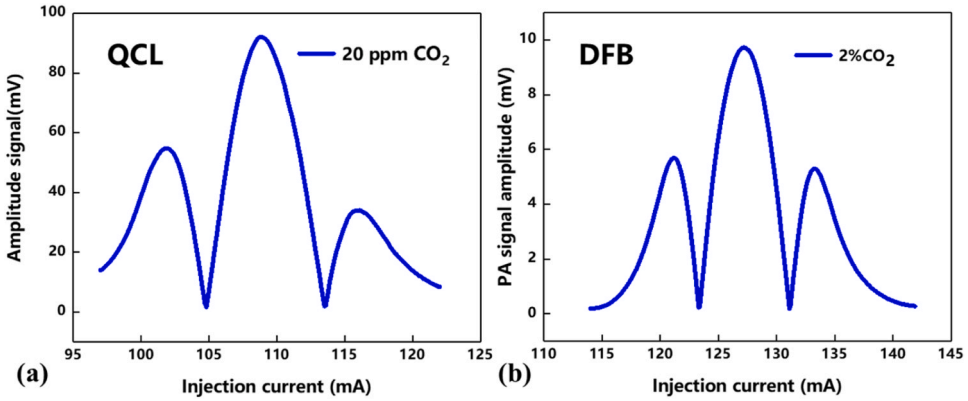


**Fig. 5.** 2f-WMPAS spectral scanning measurement. (a): 20 ppm $CO_2$ in QCL Mode (b): 2 % $CO_2$ in DFB Modulation Mode.

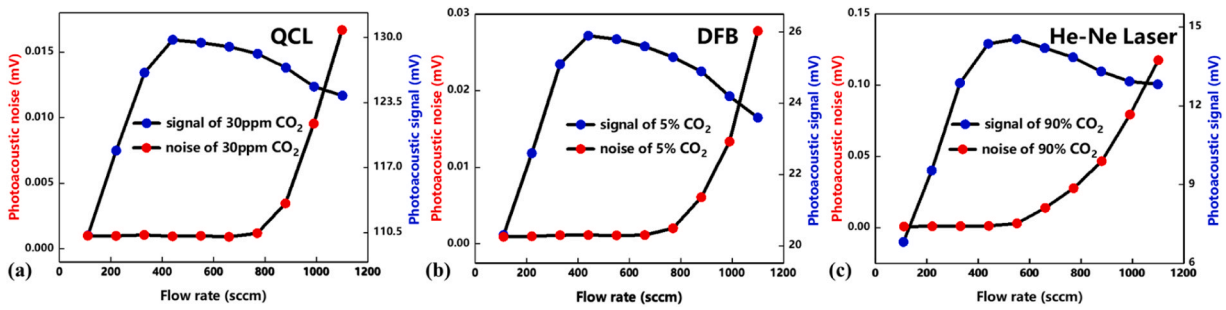


**Fig. 6.** (a), (b) and (c): The noise level and PA signals of 30 ppm, 5 % and 90 % $CO_2$ v.s. gas flow rates measured by QCL, DFB and He-Ne laser modes respectively.

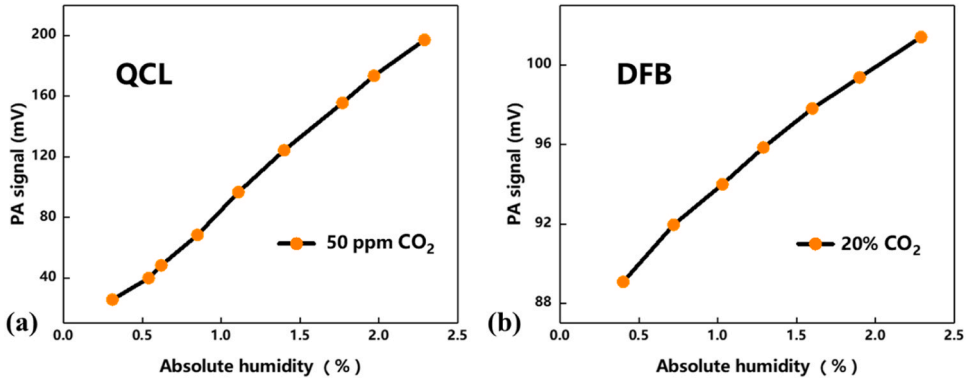


**Fig. 7.** The PA signals of 50 ppm and 20 % v.s. humidity levels measured by QCL and DFB modes.

the WMPAS signal under wet conditions originates from the energy gain of the rotational vibrational state of $N_2$. The presence of water vapor adds an additional relaxation path.

During actual measurements using the He-Ne laser, it was observed that the resonance frequency of high concentration $CO_2$ increases as humidity rises. This phenomenon occurs because the total molecular mass of the gas mixture inside the chamber decreases with the increase in humidity ($CO_2$ has a molecular mass of 44, $H_2O$ has a molecular mass of 18), which leads to an increase in the molecular gas velocity, raising the resonance frequency of the photoacoustic cell. However, the actual increasing frequency range is less than 2.5 Hz. The frequency was calibrated for humidity during the analysis, ensuring that it does not affect the accuracy of the results.

Based on the above experimental results, a humidity level of 2.2 % was selected as the final parameter of wet experiments. At this humidity level, the signal enhancement was 6.4 times for the QCL mode and 0.114 times for the DFB mode.

## 4. Results and discussions

### 4.1. Performance evaluation of the dual mode $CO_2$ sensor

To validate the performance of the dual-mode $CO_2$ sensor, the experimental parameters were set as the optimization values as described in Section 3.2. The linearity of the dual mode full-range $CO_2$ sensor was determined by testing the PA signal response for different concentrations of gases in the range 0 ppm (100 % $N_2$)-100 % $CO_2$ and the results are shown in Fig. 8.

As plotted in Fig. 8(a), the concentration-PA signal relationship for 0–80 ppm of $CO_2$, excited by the QCL, reveals a saturation concentration of 80 ppm for $CO_2$. The $R^2$ value exceeds 0.9993 within the concentration range of 0–50 ppm. As shown in Fig. 8(b), the $R^2$ value of 0.9999 indicates that the sensor has an excellent linear response to $CO_2$ concentrations below 20 %. When the concentration exceeded 20 %, the PA signal exhibited a nonlinear relationship with changing $CO_2$ concentration. Fig. 8(c) presents the concentration- resonant frequency plot

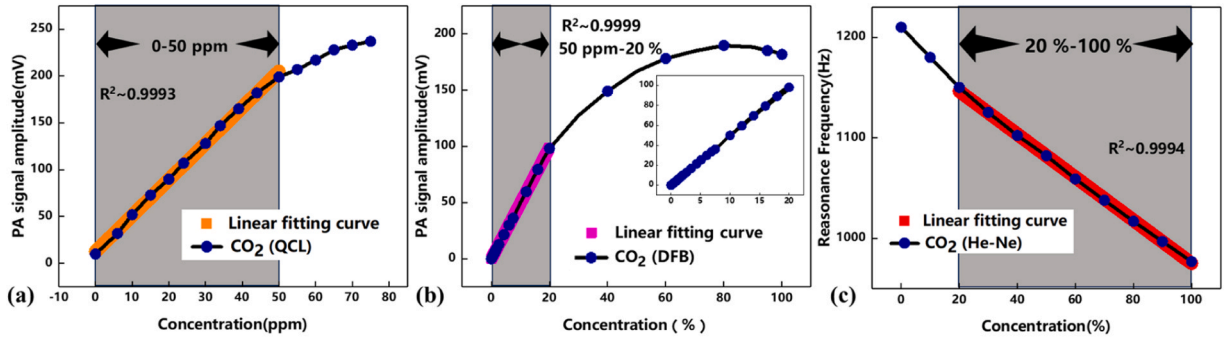


**Fig. 8.** (a) The PA signals changing with $CO_2$ concentration range from 0 ppm to 80 ppm using the QCL; (b) The PA signals changing with $CO_2$ concentration range from 0 % to 100 % using DFB (Localized enlargement of the 50ppm-20 % concentration range is shown in the small figure); (c) The resonance frequency changing with $CO_2$ concentration from 0 % to 100 % using He-Ne Laser.

covering 0–100 % using the He-Ne laser. The linear ranges of the signal were determined as 20 %-100 % with a $R^2$ value of 0.9994. A comparison of Fig. 8 and Fig. 3 shows a good agreement between the simulated and experimental curves for the QCL and DFB modes. The QCL mode becomes nonlinear beyond 50 ppm due to the high absorption at the specific absorption line, while the DFB mode exhibits nonlinearity after 20 % concentration and becomes saturated at 80 %. For the RFT mode, there are slight discrepancies between the experimental and simulated results. In the experimental data, the 0–20 % range represents low concentrations and 20 %-100 % represents high concentrations, with each showing distinct linearities. Although the experimental data for the RFT mode does not exhibit a perfect linear relationship in these ranges, the overall trend remains positive.

According to these results, the accuracy of the WMPAS technique is reduced due to photoacoustic saturation, making it difficult to accurately measure highly concentrated gases. To solve this problem, we have utilized the advantages of RFT as a complementary technology in detecting high concentration gases, thus realizing the function of full-range gas detection.

### 4.2. A continuous testing of the dual mode $CO_2$ sensor

Based on the data obtained from the above experiments as a standard, the actual measurements of concentration response in the full-range sensor were used to verify the stability and linearity of the system. In the WMPAS technique, the NNEA coefficient was used to evaluate the sensor performance [45], as defined in Eq. 3.

$$NNEA = \frac{\alpha_{\min} P_0}{\sqrt{\Delta f}} = \frac{\alpha P_0}{SNR\sqrt{\Delta f}}, \tag{3}$$

where $P_0$ represents the actual power value of the excitation light source and the remaining parameters are given in Section 2.2. $\Delta f$ is the effective integration bandwidth of the system (0.125 Hz), $\alpha_{\min}$ and $\alpha$ represent the minimum absorption coefficient and absorption coefficient of the system in succession. The SNR here indicates the ratio of signal-to-noise under specific conditions of the actual system. When the detection time was 20 s, the mean values of the QCL and DFB modes noise were found to be 1.95 μV and 2.94 μV, respectively, with standard deviations 0.95 μV and 0.99 μV, respectively.

NEC is also an important parameter for testing sensor performance [46]:

$$NEC = \frac{C}{S_{PA}/\sigma} \tag{4}$$

where C denotes the concentration of the gas to be measured, $S_{PA}$ represents the signal, defined as the photoacoustic signal amplitude minus the mean noise, and σ signifies the standard deviation of the noise.

The results of the QCL mode for actual measurements of 0–50 ppm $CO_2$ are shown in Fig. 9(a). The average value of the photoacoustic signal was 199.87 mV at 50 ppm, which reveals a NNEA of $6.31 \times 10^{-6}$ $Wcm^{-1}/\sqrt{Hz}$ and a NEC of 240 parts per trillion (ppt). Fig. 9(b) shows the concentration-signal response obtained from 50ppm to 20 % $CO_2$ measurements using the DFB laser. At 20 %, the photoacoustic signal averaged 100.31 mV, with a calculated NNEA of $4.755 \times 10^{-10}$ $Wcm^{-1}/\sqrt{Hz}$ and a NEC of 2.26 ppm. Fig. 9(c) shows the resonance frequency-signal response obtained from 20 % to 100 % $CO_2$ measurements using the He-Ne laser. The results show that the stability and linearity of the sensors are maintained at a good level.

Three environments were simulated in the laboratory: a microbial growth setting (low concentrations), a factory production environment (medium concentrations), and a metal smelting environment (high concentrations). The temperature in the simulated environment was set to 30° and the pressure was set to 1 atm. Low, medium and high concentration $CO_2$ leaks were set up according to the characteristics of each environment, and the results were continuously monitored using the compact and full-range $CO_2$ sensor, as shown in Fig. 10.

The initial mode of the sensor was the RFT mode. If the detection frequency remains below 1126 Hz (corresponding concentration is 20%), the RFT mode was enabled, otherwise it automatically switched to the DFB mode. This transition is achieved by changing the sinusoidal signal $f_1$, used for the He-Ne laser, to a sinusoidal signal with a sawtooth waveform $f_2$, which applies to the DFB. If the result of the DFB mode was below 0.0535 mV (corresponding concentration is 50 ppm), the system would switch to the QCL mode, and the conversion process is like the above, by changing the signals $f_2$ for DFB sine and sawtooth waveforms to the signals $f_3$ for QCL sine and sawtooth waveforms. The corresponding detection concentration ranges for the three modes are shown in Eq. 5

$$\begin{cases} QCL & \mathrm{mod}\, e: \quad 0 - 50ppm \\ DFB & \mathrm{mod}\, e: \quad 50ppm - 20\% \\ RFT & \mathrm{mod}\, e: \quad 20\% - 100\% \end{cases} \tag{5}$$

Fig. 10 shows the results of actual measurements with 30 ppm, 10 %, and 80 % $CO_2$ using the sensor. Pure $N_2$ (0 % $CO_2$) was first injected into the sensor, and after 20 s when it was internally stabilized, $CO_2$ with a concentration of 30 ppm was immediately injected at a flow rate of 440 sccm, and the resonance frequency was stabilized after about 5 s. It took a total of 7 s to switch to the DFB mode and complete the detection, and 8 s to switch to the QCL mode and complete the detection. The total detection time ranged from a minimum of 5 seconds to a maximum of 20 seconds, which was determined by the gas concentration.

## 5. Conclusions

A compact and laser-based dual-mode sensor was developed and confirmed to effectively detect $CO_2$ across the entire concentration range with integrated laser module excitation and self-developed optimized differential resonator.

Parameters such as the modulation depth of the QCL and DFB with

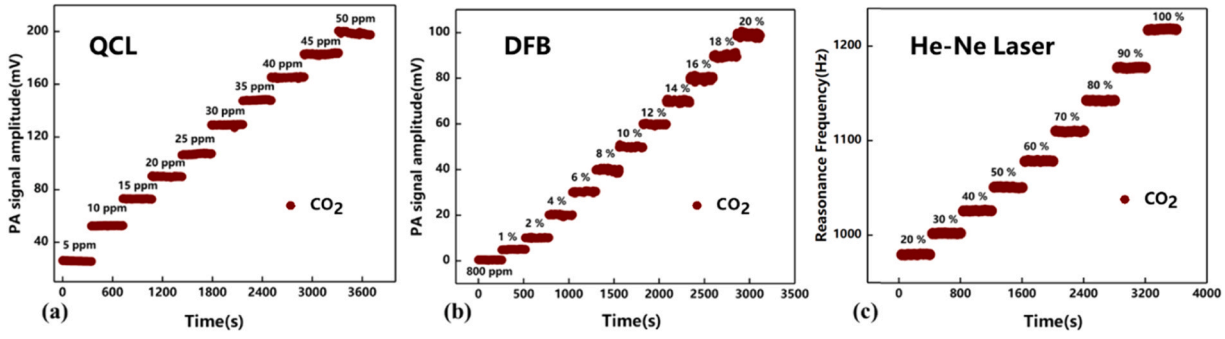


**Fig. 9.** Continuous monitoring with the compact and full-range sensor (a): QCL mode for $CO_2$ of 0–50 ppm (b): DFB mode for $CO_2$ of 50 ppm-20 % (c): RFT mode for $CO_2$ of 20 %-100 %.

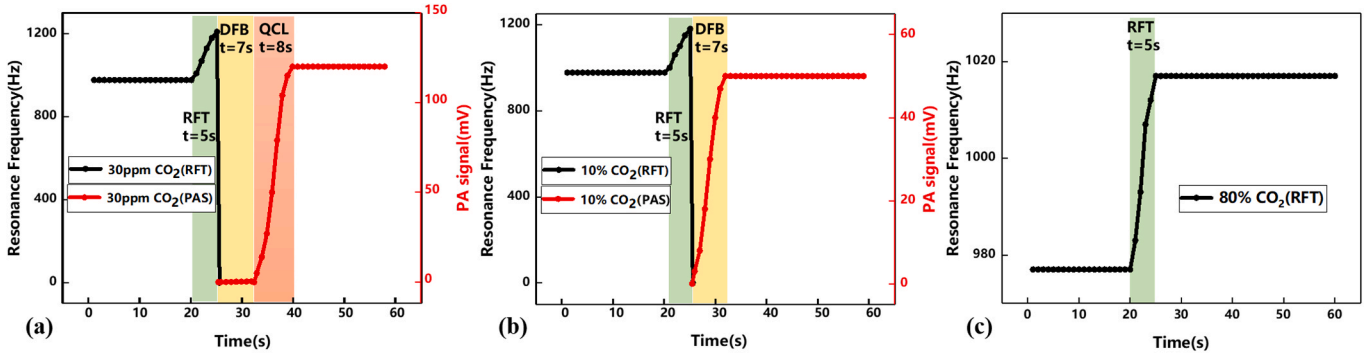


**Fig. 10.** Practical measurements with the compact and full-range sensors (a): 30 ppm $CO_2$ (b): 10 % $CO_2$ (c): 80 % $CO_2$.

second harmonic current, gas flow rate, and humidity were optimized before formal experiments. Additionally, the concentration intervals detected by each laser were determined through simulation. The QCL mode detected low concentrations (0–50 ppm), the DFB mode handled medium concentrations (50 ppm - 20 %), and the RFT mode was capable of accurately measuring high concentrations (20 % - 100 %), providing linearity to the instrumentation in this range.

In summary, the new sensor has a NEC of 240 ppt and a NNEA of $4.755 \times 10^{-10}$ $Wcm^{-1}/\sqrt{Hz}$ with an $R^2$ value of $\geq 0.9993$. The dual-mode gas sensor exhibits a fast response time of 5 seconds. Utilizing both WMPAS and RFT modes, and combining QCL and DFB sources, the sensor achieves a dynamic range of 0–20 %. Employing the RFT mode extends the linear dynamic range to 100 %. Finally, the stability and accuracy of the sensor was verified through continuous monitoring.

## CRediT authorship contribution statement

**Yifan Li:** Writing – original draft. **Lixian Liu:** Writing – review & editing. **Roberto Voti:** Conceptualization. **Andreas Mandelis:** Data curation. **Jialiang Sun:** Software. **Le Zhang:** Supervision. **Xueshi Zhang:** Validation. **Liang Zhao:** Visualization. **Xiaopeng Shao:** Funding acquisition, Formal analysis. **Jiyong Zhang:** Investigation. **Yize Liang:** Project administration, Methodology. **Huiting Huan:** Resources.

## Declaration of Competing Interest

The authors declare that they have no known competing financial interests or personal relationships that could have appeared to influence the work reported in this paper

## Acknowledgements

The authors are grateful to the National Natural Science Foundation of China (Grant Nos. 62175194, 62350710213 and 62271370). This work was also supported by the Fundamental Research Funds for the Central Universities (Grant Nos. QTZX23081 and QTZX23069). We also acknowledge the Concept Grant of Hangzhou Institute of Technology of Xidian University (No. GNYZ2023XJ0203). L. Liu acknowledges the Natural Science Foundation of Shaanxi Province (Grant No. 2023-YBSF188). This research was also supported by the Baima Lake Laboratory Joint Funds of the Zhejiang Provincial Natural Science Foundation of China under Grant No. LBMHZ24F050003. AM also gratefully acknowledges a Discovery fund from the Natural Sciences and Engineering Research Council of Canada and to Canada Foundation for Innovation (CFI) JELF program.

## Data availability

No data was used for the research described in the article.

## References

[1] A.A. Hamed, M.A. Ghareeb, A.K. Kelany, Induction of antimicrobial, antioxidant metabolites production by co-cultivation of two red-sea-sponge-associated Aspergillus sp, $CO_2$ and Bacillus sp. COBZ21. BMC Biotechnol. 24 (1) (2024) 3.
[2] S. Yu, X. Yan, Y. He, Study on the leakage morphology and temperature variations in the soil zone during large-scale buried $CO_2$ pipeline leakage, Energy 288 (2024) 129674.
[3] Y. Chong, H. Li, T. Pan, More applicable quantification of non- $CO_2$ greenhouse gas emissions from wastewater treatment plants by on-site plant-integrated measurements, Sci. Total Environ. 929 (2024) 172598.
[4] A. Arneth, P.A. Miller, M. Scholze, $CO_2$ inhibition of global terrestrial isoprene emissions: potential implications for atmospheric chemistry, Geophys. Res. Lett. 34 (18) (2007) 10–1029.
[5] M. McIntyre, B. McNeil, Morphogenetic and biochemical effects of dissolved carbon dioxide on filamentous fungi in submerged cultivation, Appl. Microbiol. Biotechnol. 50 (1998) 291–298.
[6] K. Zhou, Y. Zhang, X. Jia, Co-cultivation of fungal-microalgal strains in biogas slurry and biogas purification under different initial $CO_2$ concentrations, Sci. Rep. 8 (1) (2018) 7786.
[7] F. Zadrazil, Influence of $CO_2$ concentration on the mycelium growth of three Pleurotus species, Eur. J. Appl. Microbiol. 1 (4) (1975) 327–335.
[8] Y. Xu, M. Zhang, J. Long, Co single atom modulating the secondary coordination environment of Bi sites for boosting the adsorptive and catalytic capacity during $CO_2$ photoreduction, Appl. Catal. B: Environ. 340 (2024) 123230.
[9] E.A. Robinson, G.D. Ryan, J.A. Newman, A meta-analytical review of the effects of elevated $CO_2$ on plant–arthropod interactions highlights the importance of interacting environmental and biological variables, N. Phytol. 194 (2) (2012) 321–336.
[10] J.F. Weltzin, R.T. Belote, N.J. Sanders, Biological invaders in a greenhouse world: will elevated $CO_2$ fuel plant invasions, Front. Ecol. Environ. 1 (3) (2003) 146–153.
[11] A.R. Oliveira, C. Mota, G. Vilela-Alves, An allosteric redox switch involved in oxygen protection in a CO2 reductase, Nat. Chem. Biol. 20 (1) (2024) 111–119.
[12] M.U. Sieborg, J.M.S. Oliveira, L.D.M. Ottosen, Flue-to-fuel: bio-integrated carbon capture and utilization of dilute carbon dioxide gas streams to renewable methane, Energy Convers. Manag. 302 (2024) 118090.
[13] C.F. You, X.C. Xu, Coal combustion and its pollution control in China, Energy 35 (11) (2010) 4467–4472.
[14] P.S. Murvay, I. Silea, A survey on gas leak detection and localization techniques, J. Loss Prev. Process Ind. 25 (6) (2012) 966–973.
[15] N. Zhang, C. Liu, C. Hou, The impact of indoor carbon dioxide exposure on human brain activity: a systematic review and meta-analysis based on studies utilizing electroencephalogram signals, Build. Environ. 259 (2024) 111687.
[16] F.A. Rahman, M.M.A. Aziz, R. Saidur, Pollution to solution: capture and sequestration of carbon dioxide ($CO_2$) and its utilization as a renewable energy source for a sustainable future, Renew. Sustain. Energy Rev. 71 (2017) 112–126.
[17] Y.S. Liu, Y. Cao, J.J. Hou, Identifying common paths of $CO_2$ and air pollutants emissions in China, J. Clean. Prod. 256 (2020) 120599.
[18] Y. Tong, X. Liao, Y. He, Mitigating greenhouse gas emissions from municipal wastewater treatment in China, Environ. Sci. Ecotechnol. 20 (2024) 100341.
[19] N. Aziz, B. Hossain, L. Lamb, The effectiveness of environmental protection policies on greenhouse gas emissions, J. Clean. Prod. 450 (2024) 141868.
[20] S. Ma, N. Deng, C. Zhao, Decreasing Greenhouse Gas Emissions from the Municipal Solid Waste Sector in Chinese Cites, Environmental Science & Technology, 2024.
[21] S. Zhang, J. Zhang, Z. Wang, Advancements in oxygen blast furnace technology and its application in the smelting of vanadium-titanium magnetite: a comprehensive review, Miner. Eng. 212 (2024) 108732.
[22] B. Han, C. Gao, Y. Li, Energy saving analysis for $CO_2$–$O_2$ mixed injection technology in converter steelmaking, J. Iron Steel Res. Int. 31 (2024) 1095–1103.
[23] Z. Zhao, X. Yu, Y. Shen, Numerical study of the feasibility of injecting $CO_2$-containing off-gas in an ironmaking blast furnace, Fuel 361 (2024) 130648.
[24] K.D. Bartle, P. Myers, History of gas chromatography, TrAC Trends Anal. Chem. 21 (9-10) (2002) 547–557.
[25] R. Ariyaratne, M.A. Elangasinghe, M.L. Zamora, Understanding the effect of temperature and relative humidity on sensor sensitivities in field environments and

improving the calibration models of multiple electrochemical carbon monoxide (CO) sensors in a tropical environment, Sens. Actuators B: Chem. 390 (2023) 133935.
[26] A. Dey, Semiconductor metal oxide gas sensors: a review, Mater. Sci. Eng.: B 229 (2018) 206–217.
[27] A. Hosoya, S. Tamura, N. Imanaka, A catalytic combustion-type carbon monoxide gas sensor incorporating an apatite-type oxide, ISIJ Int. 56 (9) (2016) 1634–1637.
[28] L. Zhang, L. Liu, X. Zhang, T-type cell mediated photoacoustic spectroscopy for simultaneous detection of multi-component gases based on triple resonance modality, Photoacoustics 31 (2023) 100492.
[29] J. Sun, B. Liu, L. Liu, Multicomponent gas sensors based on photoacoustic spectroscopy technology: a review, Microw. Opt. Technol. Lett. 66 (2) (2024) 34039.
[30] Lixian LIU, Baisong CHEN, ZHANG, Le, Simultaneous detection of multi-component trace gases by photoacoustic spectroscopy for industrial parks, Phys. Lett. 71 (17) (2022) 170701.
[31] X. Zhang, L. Liu, L. Zhang, A compact portable photoacoustic spectroscopy sensor for multiple trace gas detection, J. Appl. Phys. 131 (2022) 174501.
[32] L. Liu, H. Huan, A. Mandelis, Design and structural optimization of T-resonators for highly sensitive photoacoustic trace gas detection, Opt. Laser Technol. 148 (2022) 107695.
[33] I.E. Gordon, L.S. Rothman, R.J. Hargreaves, The HITRAN2020 molecular spectroscopic database, J. Quant. Spectrosc. Radiat. Transf. 277 (2022) 107949.
[34] Hongpeng Wu, Enhanced near-infrared QEPAS sensor for sub-ppm level H2S detection by means of a fiber amplified 1582 nm DFB laser, Sens. Actuators B: Chem. 221 (2015) 666–672.
[35] Kumar Kinjalk, Highly selective and sensitive detection of volatile organic compounds using long wavelength InAs-based quantum cascade lasers through quartz-enhanced photoacoustic spectroscopy, Appl. Phys. Rev. 11 (2024) 021427.
[36] A. Rosencwaig, Theoretical aspects of photoacoustic spectroscopy, J. Appl. Phys. 49 (5) (1978) 2905–2910.
[37] X. Han, C. Li, M. Guo, Fiber-optic trace gas sensing based on graphite excited photoacoustic wave, Sens. Actuators B: Chem. 408 (2024) 135546.
[38] L. Liu, H. Huan, X. Zhang, Laser induced thermoelastic contributions from windows to signal background in a photoacoustic cell, Photoacoustics 22 (2021) 100257.
[39] B. Huan, H. Huan, L. Liu, Sensitivity dependence of optical parameters in a photoacoustic cell analyzed with a 2-D thermoelastic approximation, Opt. Commun. 497 (2021) 127171.
[40] L. Liu, H. Huan, W. Li, Highly sensitive broadband differential infrared photoacoustic spectroscopy with wavelet denoising algorithm for trace gas detection, Photoacoustics 21 (2021) 100228.
[41] J.P. Besson, S. Schilt, L. Thevenaz, Sub-ppm multi-gas photoacoustic sensor, Spectrochim. Acta A 63 (2006) 899–904.
[42] L. Liu, H. Huan, X. Zhang, Wavelength-modulated photoacoustic spectroscopic instrumentation system for multiple greenhouse gas detection and in-field application in the Qinling mountainous region of China, Photoacoustics 38 (2024) 100620.
[43] J. Wang, M. Chen, Q. Chen, Photoacoustic spectrometry and resonant frequency tracking based dual-mode gas sensor, Sens. Actuators B: Chem. 390 (2023) 133796.
[44] G. Wysocki, A.A. Kosterev, F.K. Tittel, Influence of molecular relaxation dynamics on quartz-enhanced photoacoustic detection of CO 2 at λ= 2 μm, Appl. Phys. B 85 (2006) 301–306.
[45] Wu Hongpeng, Research on new quartz enhanced photoacoustic spectroscopy technology, Shanxi University, Shanxi, 2017.
[46] L.I. Zhengang, S.I. Ganshang, N.I.N.G. Zhiqiang, Photoacoustic detection of $CO_2$ based on mid-infrared LED, J. Opt. 42 (13) (2022) 206–215.

**Yifan Li** is a master student at the School of Physics and Optoelectronic Engineering, Xidian University. She focuses on the high sensitivity and large range gas detection technology.

**Lixian Liu** received her B.S. degree of electronic science and technology and doctorate in optical engineering from the University of Electronic Science and Technology of China, in 2012 and 2017, respectively. She is now a full-time associate professor in the School of Physics and Optoelectronic Engineering, Xidian University. Her research field is photoacoustic and optical spectroscopy technologies.

**Liang Zhao** was born in Shaanxi, China, in May 1983. He received the B.E. and Ph.D. degrees in Physical electronics from Xi'an Jiaotong University in 2006 and 2012, respectively. Since 2006, he has been with Northwest Institute of Nuclear Technology (NINT), Xi'an, China. He has published over 50 journal articles and proceeding papers. His research interests include solid insulation, vacuum insulation and the pulsed power technology.

**Xueshi Zhang** is a Ph.D student at the School of Physics and Optoelectronic Engineering, Xidian University. He focuses on the high sensitivity trace gas detection technology.

**Le Zhang** is a Ph.D. student at the School of Physics and Optoelectronic Engineering, Xidian University. His research interests include photoacoustic spectroscopy and its application to trace gas detection.

**Jialiang Sun** is a master student at Xidian University of Hangzhou Institute of Technology. He focuses on the research direction of high-precision photoacoustic spectroscopy and multi-component gases.

**Huiting Huan** received his B.S. and Ph.D degrees from the University of Electronic Science and Technology of China in 2012 and 2017, respectively. He is now a researcher and associate professor with the School of Mechano-Electronic Engineering, Xidian University. His main research field includes acoustic, electromagnetic and thermal radiometric nondestructive testing.

**Yize Liang** received his B.S. degree of optoelectronic information science and engineering and doctorate in optical engineering from Huazhong University of Science and Technology, in 2018 and 2023. He is now an assistant professor in the School of Optoelectronic Engineering, Xidian University. His research field includes structured light, multi-mode fiber and free-space optics.

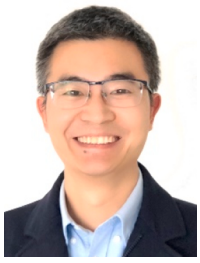

**Jiyong Zhang** received his Ph.D. degree in Computer Science from Swiss Federal Institute of Technology at Lausanne(EPFL) in 2008. He received his B.S. degree and M.S. degree in Computer Science from Tsinghua University in 1999 and 2001 respectively. He is currently a full-time professor in Hangzhou Dianzi University. His research interests include artificial intelligence, machine learning, data mining and image processing.

**Xiaopeng Shao** received his Ph.D degree from Xidian University in 2005. He is a professor at the School of Physics and Optoelectronic Engineering, Xidian University. His research focuses on computational imaging, optical sensing and signal processing.

**Andreas Mandelis** received his B.S. degree in physics from Yale University, New Haven, CT, USA in 1974, followed by M. A., M.S.E., and Ph.D degrees in applied physics and materials science from Princeton University, Princeton, NJ, USA in 1976, 1977 and 1979, respectively. He is a Full Professor of mechanical and industrial engineering; electrical and computer engineering; and the Institute of Biomaterials and Biomedical Engineering, University of Toronto, Toronto, ON, Canada. He is the Director of the Center for Advanced Diffusion-Wave and Photoacoustic Technologies (CADIPT), Toronto. He is an author and coauthor of more than 410 scientific papers in refereed journals and 190 scientific and technical proceedings papers. He is the Editor-in-Chief of the Springer Nature International Journal of Thermophysics, and an Editor of the Journal of Biomedical Optics and the Journal of Applied Physics.

**Prof. Roberto Li Voti** is currently Full Professor in Physics at Sapienza University of Rome, Italy. From 2023 is Head of Department of Basic and Applied Science for Engineering—Engineering Faculty, at the same University. From 2023 is Director of Master in Optics and Quantum Information. In 2020 and 2021, he was also a specially appointed Professor at the Tokyo Institute of Technology, Tokyo, Japan. He is author of more than 200 scientific papers in the areas of optics, photothermal and photoacoustic techniques for nondestructive testing of materials. From 2019–2023 served as Associate Editor for the International Journal of Thermophysics. In 2019, 2021, and 2023, he was the Co-Chair of Joint Symposia at CLEO/Europe-EQEC in Munich. Since 2010, he is the Director of the biennual Courses of Photoacoustic and Photothermal Techniques at International School of Quantum Electronics in Erice (Sicily) at the Ettore Majorana Foundation and Centre for Scientific Culture (EMFCSC). From 2024 he is also in the board of Directors of the International Photoacoustic and Photothermal Association (IPPA).